Inter-well scale natural fracture geometry and permeability variations in low-deformation carbonate rocks

Bisdom, K.; Bertotti, G.; Bezerra, F. H.

DOI
10.1016/j.jsg.2017.02.011

Publication date
2017

Document Version
Accepted author manuscript

Published in
Journal of Structural Geology

Postprint of Journal of Structural Geology
Volume 97, April 2017, Pages 23–36
Link to formal publication (Elsevier): http://dx.doi.org/10.1016/j.jsg.2017.02.011

Inter-well scale natural fracture geometry and permeability variations in low-deformation carbonate rocks

K. Bisdom[1], G. Bertotti[1], F.H. Bezerra[2]

1) Department of Geoscience & Engineering, Delft University of Technology, Delft, Netherlands

2) Departamento de Geologia, Programa de Pós-Graduação em Geodinâmica e Geofísica, Universidade Federal do Rio Grande do Norte, Natal, Brazil

Keywords: natural fractures, equivalent permeability, aperture, discrete fracture networks, Potiguar basin, shallow-water carbonates

Abstract

Regional natural fracture networks often show variations on a scale below that captured by seismic reflection data. This variability is not considered in most reservoir models, but likely impacts uncertainties in permeability. We quantify this uncertainty using a database of 13,000 fractures in nine outcrops digitised in the carbonate Jandaíra Formation (Potiguar basin, Brazil). Distance between outcrops is on average 11 km, with a minimum of 300 m, which is comparable to the distance between wells in naturally fractured reservoirs. In between outcrops, significant variations exist in orientation, intensity, length and topology. Using discrete fracture-matrix flow models, we model the permeability of each deterministic pattern and find that small changes in geometry and topology result in permeability variations that are not captured by connectivity-based analyses such as percolation probabilities, particularly when the matrix is permeable. The permeability variations associated with subseismic-scale fracture variability are not captured in conventional stochastic models, but can be captured using deterministic outcrop models with flow through discrete fractures. The deterministic models provide a permeability range associated with subseismic fracture variability, that can

be assigned to grid cells of fractured reservoir flow models, as an alternative to assuming constant permeability in the absence of subseismic-scale deformation.

1. Introduction

Wells in naturally fractured reservoirs produce from multiscale fracture systems that are partly or completely below the resolution of seismic reflection data (Bonnet et al., 2001; Makel, 2007). Natural fractures can be measured in wells, but these data typically only provide a 1-D, or 3-D in the case of borehole images, characterisation that does not fully capture the spatial and size distributions of 3-D fracture networks at scales larger than the borehole (Bourbiaux et al., 2002; Gauthier et al., 2002). The existence of common heterogeneities in fracture networks is well-known from large-scale outcrops of fractured rocks, such as those in the Bristol Channel in the UK or the Burren in Ireland (Cosgrove, 2001; Gillespie et al., 2001; Belayneh and Cosgrove, 2010). Overall spatial trends in geometry with associated porosity and permeability are often captured in reservoir models by relating fracture orientation and intensity to characteristics and development history of larger-scale host structures such as folds or faults (Price, 1966; Bergbauer, 2007; Smart et al., 2009; Shackleton et al., 2011).

Relations between seismic-scale deformation and fracture networks help to capture km-scale trends in fracture intensity and orientation that are observed in some reservoirs, but outcrops typically indicate that, at a subseismic scale, variability of fracture network geometry does not simply relate to the geometry of the larger, seismic-scale folds or faults (Bisdom et al., 2014). With respect to this matter, we focus on fractured carbonate reservoirs that experienced very little tectonic deformation and consider the inter-well scale (i.e. several hundred metres to less than ten kilometres), where fracture variability is not easily quantified, but may impact permeability (Peacock, 2006; Lei and Wang, 2016). Obtaining a better

49 understanding of the impact of this scale of fracture variability on permeability should help to
50 quantify appropriate uncertainty ranges for permeability that otherwise can often not be
51 entirely quantified in subsurface datasets (Belayneh et al., 2009). The impact of subseismic-
52 scale variability in network geometry on permeability has been studied before, particularly
53 for the assessment of leakage risks for storage of CO_2 and nuclear waste, where even a small
54 subset of conductive fractures poses significant risks (Long and Billaux, 1987; Nussbaum et
55 al., 2011; Bond et al., 2013). These studies require high-resolution datasets of subseismic
56 fracture networks, which can sometimes be characterised from subsurface datasets provided
57 that data are available from a dense network of wells (Bond et al., 2013), or from subsurface
58 study sites (Long and Billaux, 1987; Nussbaum et al., 2011; Follin et al., 2014; Laurich et al.,
59 2014). These subsurface sites provide exposures on the scale of metres, but to incorporate
60 datasets that better constrain the issue, uninterrupted exposures of fracture networks covering
61 several hundred by several hundred metres are needed. To our knowledge, no studies have
62 used such large exposures to focus explicitly on the variability in fracture network
63 characteristics at the scale of the domain between wells in a typical fractured reservoir, for
64 flow modelling through deterministic fracture patterns without any stochastic component.

65 Conventional workflows for modelling permeability in fractured reservoir models can
66 be based on extracting geometrical distributions from outcrops for stochastic Discrete
67 Fracture Networks (DFNs) and upscaling to effective properties, where seismic-scale
68 variability in fracture patterns is constrained by considering the resultant structural
69 geometries and implications of kinematic and mechanical forward models (Sanders et al.,
70 2004; Shackleton et al., 2009; Bond et al., 2013; Watkins et al., 2015; Ukar et al., 2016).
71 Subseismic trends in fracture network geometry on permeability have been studied in
72 outcrops, both with and without matrix flow, albeit without application to DFNs (Odling,
73 1997, 2001; Odling et al., 1999). These works found that in addition to density and

orientation, connectivity impacts permeability, even if fractures are disconnected (Odling and Roden, 1997). Stochastic DFNs are ideal for subsurface datasets, where typically 1-D fracture geometry distributions are available that need to be extrapolated to 3-D reservoir models, but they are less apt at representing the variability in outcrop-scale fracture geometry, as for example, they do not allow for the control that older fractures have on the geometry of younger fractures and they typically consider fractures as purely straight segments (e.g. Belayneh et al., 2009; Bonneau et al., 2016a; Hardebol et al., 2015). This limitation can be partly overcome by combining stochastic models with rules for the generation of the fracture network based on geomechanical requirements for fracture formation (Bonneau et al., 2016). Alternatively, we propose to use deterministic networks digitised from 2-D outcrops that capture the natural variability and complexity of fracture networks for inclusion in the permeability-focused models. We use actual patterns from closely-spaced outcrops in a setting where the regional stress and lithological boundary conditions were approximately constant, to quantify the impact of fracture network variability on permeability variability.

The datasets are acquired from the Jandaíra Formation in the Potiguar basin (NE Brazil), which is a flat-lying carbonate that is exposed in km-scale outcrops in the region south and west of the city of Mossoró (Figure 1). The post-rift formations have experienced limited faulting and folding, but the regional fracture network nonetheless has a high intensity (de Graaf et al., 2017). Whereas syn-rift deformation in the region is influenced by pre-existing basement faults, these relations seem mostly absent for fracture networks in the younger and shallower Jandaíra Formation (Kirkpatrick et al., 2013; Soden et al., 2014). We collect a multiscale dataset of fracture geometries using an Unmanned Aerial Vehicle (UAV) to image the large outcrops, combined with photogrammetry to construct georeferenced outcrop images. A total area of 8.8×10^5 m^2 is covered, where fracture length scales between 0.1-300 m are captured. The minimum distance between outcrops is 300 m.

We use this unique dataset to quantify the implications for permeability in Naturally Fractured Reservoir (NFR) flow modelling, focusing on uncertainties related to i) Inter-well, subseismic-scale natural variations in fracture network geometry; and ii) The impact of matrix permeability on the validity of geometry-based percolation methods. The aim is to provide an improved understanding of the quantitative impact of these uncertainties for permeability determined from subsurface NFR modelling workflows, focusing on the inter-well scale, which normally lacks direct measurements of fracture geometry and permeability.

Flow is modelled using Discrete Fracture and Matrix (DFM) models (Matthäi and Nick, 2009; Geiger et al., 2010). Contrary to Discrete Fracture Network (DFN) models, which do not consider flow through the matrix, we consider the possible flow exchange between fractures and a permeable matrix. This additional consideration incorporates flow contributions from fractures disconnected from the main percolating network (Nick et al., 2011; Bisdom et al., 2016c). As the apertures of the outcropping fractures are not representative of the apertures that would be present in the subsurface fractures due to ambient stress conditions, we use geomechanical stress-aperture models to provide apertures for our networks (Bisdom et al., 2016a). The resulting permeability is summarised as equivalent permeability in 2-D, which can be compared to the effective permeability of grid cells in conventional reservoir flow models (Matthäi and Belayneh, 2004; Matthäi et al., 2007; Matthäi and Nick, 2009). This equivalent permeability captures matrix and fracture flow combined in a single parameter, including sub-gridcell trends in fracture permeability associated with geometry variations. These variations are less easily captured in conventional fracture flow modelling approaches based on the ODA method (Oda, 1985). Moreover, ODA-based methods require the use of dual-permeability grids.

We also compare these results with predictions made by percolation methods, which are often applied to predict the reservoir permeability associated with a DFN geometry

(Robinson, 1983, 1984; Berkowitz and Balberg, 1993; de Dreuzy et al., 2000; Berkowitz, 2002). These analytical methods are computationally inexpensive and can be applied to reservoir-scale DFNs, but as percolation is only an indirect proxy for flow, it may not always yield representative results. Using our DFM models, we define the fracture network geometries and matrix conditions for which percolation accurately describes the permeability modelled using the DFMs.

2. Geological setting

The Potiguar basin is a rift basin in NE Brazil, formed during the crustal break-up of Gondwana (Ojeda, 1982; Matos, 1992). The onshore part of the basin has a width of 350 km, measured along the coast, and consists of several NE-SW trending grabens that continue 200 km inland, with individual widths of 100 km (Figure 1) (Reis et al., 2013).

2.1. Tectonics

The basin is part of the Equatorial Atlantic, a shear margin that connects the south and central Atlantic (Matos, 1992). It is one of three NE-SW trending intracontinental basins in NE Brazil, which are bounded by transfer faults (Brito Neves et al., 1984). Basin-scale NE-SW striking basement faults define the structure of the main horst and grabens of the Potiguar basin (Matos, 1992; Reis et al., 2013). Rifting started in the Early Cretaceous, followed by a post-rift transition phase in the Aptian and a drift phase from the Albian onward (Reis et al., 2013). Maximum burial of the post-rift Jandaíra Formation is difficult to constrain but, based on Fourier Power Spectrum analysis of burial-related horizontal stylolites it is found to be less than 1500 m in the study area (Ebner et al., 2009; de Graaf et al., 2017).

Uplift of the post-rift sediments started in the Cenozoic (Bezerra and Vita-Finzi, 2000; Gurgel et al., 2013). At present, the basin is experiencing a strike-slip regime where a maximum horizontal stress strikes E-W in the east of the basin and rotates to NW-SE in the

western part (Assumpção, 1992; Bezerra et al., 2007). Within the area of interest in the western part of the basin, NW-SE and NE-SW striking faults are present, but these faults are not known to be active as a result of the present regional stress field (Reis et al., 2013). Also, the studied rock pavements of the post-rift Jandaíra Formation dip consistently sub-horizontally at about 3°, indicating that these exposed layers in this part of the basin have not been folded (Figure 1).

2.2. Stratigraphy

Post-rift deposition started with the Albian Açu Formation, which consists of fluvial-estuarine sandstones and mudstones (Ojeda, 1982). This non-marine phase was followed by transgression and deposition of the Jandaíra carbonate platform from the Turonian to Campanian (Matos, 1992). The Jandaíra Formation consists of mudstones, packstones and grainstones with a depositional thickness of up to 700 m in the onshore part of the basin (Fernandes et al., 2015; Santos Filho et al., 2015). Most of the studied outcrops are composed of packstones-grainstones with only small variations in grain size, except for two outcrops (Mossoró 1 and 2 in Figure 1) in the northwest, where the lithology is mainly dominated by mudstones. Bedding orientation in all outcrops is sub-horizontal, with an average dip of 3° towards the north and a scatter of less than 3°. Within most outcrops, only a single stratigraphic layer is exposed, but limited vertical exposures and Ground Penetrating Radar data show that the lithology is relatively constant in vertical and horizontal directions (Fernandes et al., 2015).

3. Fracture network analysis

Outcrops in the basin show heterogeneous fracture patterns, even though lithology is mostly constant, layers are sub-horizontal and most outcrops consist of a single stratigraphic layer with no significant changes in bedding (Figure 2a). The outcrops contain bed-perpendicular

fractures, often with indications of mixed shearing and opening-mode deformation (Figure 2b), and both tectonic and burial-related stylolites (Figure 2c,d).

3.1. Data acquisition and database

Mapping of the fracture networks was done through a multiscale approach combining UAV imagery and measurements at the outcrop surface. The UAV is a multi-rotor vehicle equipped with a compact camera and positioning sensors. During 20-minute pre-programmed flights at an altitude of 50 m above the outcrops, between 100 and 150 images with more than 50% overlap were taken of areas up to 200 x 200 m. At this altitude, the image resolution of our camera is 1.4 cm/px, which is sufficient to capture the barren fracture network (i.e. fractures that presently have a visible aperture). Features such as stylolites and veins without colour variation could not be resolved consistently in this imagery, as most outcrops are weathered, creating clints and grikes (Figure 2e) (Jones, 1965).

The UAV images were merged into georeferenced orthomosaics using photogrammetry software (Agisoft® PhotoScan®). Georeferencing was done using positioning sensors in the UAV and outcrop markers measured by laser range finders or GNSS (Global Navigation Satellite System). Fractures were manually digitised using the GIS-based software DigiFract (Hardebol and Bertotti, 2013), from which length, orientation and spatial distributions were extracted. For mutually crosscutting fractures, which are abundant, length was defined from fracture end-point to end-point. Fracture digitisation was done manually to ensure that individual fractures were accurately represented, instead of using automatic interpretation methods, which are typically faster, but introduce artefacts into the fracture trace network due to the software algorithms (Kemeny and Post, 2003; Hodgetts, 2013; Vasuki et al., 2014).

Using the UAV imaging approach, we digitised nine outcrops that cover a total area of 8.8×10^5 m^2, with individual outcrops sizes between 1.6×10^4 - 2.1×10^5 m^2. The outcrops are mostly in the western part of the basin, which we further subdivide into three regions (Figure 1):

1. Two *Mossoró* outcrops, west of the city of Mossoró, are in the central part of the basin.
2. Five *Apodi* outcrops, north of the town of Apodi, are closer to the southern edge of the basin.
3. Two *Dix-Sept* outcrops are in between Apodi and the town of Dix-Sept Rosado, and are slightly more towards the centre of the basin compared to the Apodi outcrops.

The total dataset consists of 13,223 fractures. Each outcrop contains between 500-2600 fractures covering three orders of magnitude for length and intensity.

3.2. Spatial variations in outcrop geometries

3.2.1. Orientation

The combined orientation distribution of the entire dataset shows a distinct N-S and a lesser E-W fracture trend, particularly when considering length-weighted orientation data. These trends represent 55% of the total orientation population (Figure 3). Three out of nine outcrops contain predominantly fractures with the N-S and E-W orientations (Apodi 3-4 and Dix-Sept 1), but the distribution is more scattered in the other outcrops (Figure 3b). Spatially, orientation does not show a systematic trend between the different outcrops.

3.2.2. Length

Fracture length varies strongly across the basin (Figure 4a). Average length varies from 17.4 m (Apodi 1) to 3.5 m (Mossoró 1), with the smallest average lengths in the Mossoró outcrops (Figure 4). This difference is not related to sampling artefacts as most outcrops have similar

219 dimensions and all images were acquired from a constant altitude, ensuring constant image
220 resolution. Still, while the variation in average length is about a factor of five, it is not
221 geographically systematic (Figure 4a-d).

222 Length was further analysed using frequency and cumulative frequency distributions
223 (Figure 4b-e). We use a density frequency distribution for the entire dataset, which is more
224 representative than cumulative frequency distributions (Bonnet et al., 2001), but the
225 individual outcrops were analysed using cumulative distributions because they do not contain
226 sufficient fractures for density distributions. Although the outcrop images cover areas of up to
227 $2x10^5$ m^2 with a resolution sufficiently high to trace fractures as small as 10 cm, the deviation
228 from the straight segments in the log-log plots indicate that the fracture length distributions
229 suffer from censoring and truncation artefacts (Figure 4b-e). Although some fractures with
230 lengths down to 10 cm have been interpreted in the images, not all fractures of this length
231 scale could be interpreted, resulting in truncation artefacts (Ortega et al., 2006). For
232 cumulative length distributions of individual outcrops, the truncation limit can be as large as
233 10 m (Apodi 2 in Figure 4b) and the censoring limit is down to 60 m (Dix-Sept 2 in Figure
234 4c). However, for all fractures from all outcrops combined, a density frequency distribution is
235 derived that covers length scales between 2 and 100 m with no censoring or truncation
236 (Figure 4e). The cumulative length frequency distribution for individual outcrops indicates
237 that for the part of the distribution that is not censored or truncated, a power-law function best
238 fits the data (Figure 4b-d). The individual exponents are close to 2.0, with the exception of
239 Apodi 3 and Mossoró 1-2, which have exponents between 2.1 and 2.3 (Figure 4a). The
240 fracture length distribution for the entire dataset from all outcrops combined is studied by
241 plotting the entire dataset in a density frequency distribution, constructed by dividing the
242 dataset into linear bins of lengths (Bonnet et al., 2001). The frequency distribution of all
243 measured fractures in the basin, filtered for censoring and truncation artefacts, follows a

power-law scaling distribution with a relatively high exponent of 2.4 (Figure 4e). Since the length domain that is not censored or truncated in the frequency and cumulative frequency distributions is limited to less than three orders of magnitude, we cannot determine whether the variability is natural or related to the artefacts, even though the original dataset covers more than four orders of magnitude in length. Because of censoring and truncation, stochastic DFN models based on these 1-D distributions use only part of the original dataset. However, for our deterministic models, all digitised fractures are included, in addition to a permeable matrix to take into account the smaller fractures that are not digitised.

3.2.3. Fracture intensity

The spatial distribution is defined by P_{21} intensity (Dershowitz and Einstein, 1988), which is defined as the cumulative length of fractures within a given area (Wu and Pollard, 2002). We use the box-counting method to define the spatial distribution (Bonnet et al., 2001), where each outcrop is discretised by a rectangular grid containing several thousand cells. The P_{21} intensity is calculated within each cell and the resulting distribution is plotted in frequency and cumulative frequency distributions (La Pointe, 1988; Walsh and Watterson, 1993; Bonnet et al., 2001; Darcel, 2003).

On average, P_{21} is close to 0.19 m^{-1} (Figure 5). Intensity is least in Apodi 5 at 0.06 m^{-1} and greatest in Dix-Sept 1 at 0.31 m^{-1}. Intensity in the other outcrops ranges between 0.13-0.21 m^{-1}, without apparent spatial trends in between outcrops across the basin.

3.2.4. Connectivity

P_{21} intensity is more representative of the spatial fracture distribution compared to P_{10}, which is typically used to define intensity in cores and along scanlines. However, neither definition

considers the spatial arrangement of fractures or whether the fractures form a percolating network for flow. To consider the connectivity of the network to measure percolation, we define percolation probability as the ratio between the number of intersections and the number of fractures, normalised for the outcrop area, where a greater value indicates a greater percolation probability (Robinson, 1983, 1984; Berkowitz, 1995; de Dreuzy et al., 2002).

The percolation probability is relatively large in outcrops with scattered orientation distributions (e.g. Apodi 1-2 and Dix-Sept 1), which is to be expected because a larger scatter in orientation increases the likelihood of fractures intersecting (Figure 6a vs. Figure 3c). This likelihood also increases when fractures are relatively long, such as in Apodi 1 and Apodi 2, but overall no relation exists between percolation probability and average length or P_{21} (Figure 6b). The percolation probability is greatest in Apodi 5, which has the smallest P_{21} intensity (Figure 6b). Similarly, Dix-Sept 2 and Mossoró 2 have the smallest percolation probabilities but average intensities compared to other outcrops (Figure 5 vs. Figure 6b).

In addition to variations in intensity and percolation, we have described heterogeneous length and orientation distributions in different parts of the basin (Table 1). These variations cannot be related to regional trends in the basin or seismic-scale structural features. However, the geometry variations are sufficiently large to likely impact permeability, and therefore need to be accounted for in models that consider the flow properties of a reservoir that hosts such a fracture population. Conventional stochastic DFNs do not typically consider these variations.

4. Impact of intrinsic fracture network variability on permeability

The digitised fracture networks form a database of structural variation at about the scale of inter-well spacing in fractured reservoirs. Although all outcrops experienced the same

292 tectonic history, we observe a large scatter in geometric characteristics from one outcrop to
293 another which cannot be linked to explanations that could be generated by considering
294 regional deformation or lithology variations. In some outcrops, the dominant fracture
295 orientations are aligned to nearby faults, such as WSW- and WNW-striking fractures in
296 Apodi 1 and 2 respectively, and SE and NE striking fractures in Apodi 5 (Figure 3).
297 However, the majority of fractures in most outcrops are not aligned with nearby faults.
298 Similarly, fracture size or intensity are not a function of distance to the regional faults (Figure
299 4 and Figure 5). We therefore attribute these geometric variations to factors that operated at
300 the subseismic scale and could vary locally, such as stress perturbations associated with stress
301 shadows of existing fractures that influence and perturb the development of subsequent
302 fractures.

303 Using DFM models, we quantify the impact of this variability on permeability. In
304 addition, we compare the results with the percolation probabilities. Four fracture networks are
305 selected for fluid-flow modelling. The characteristics that they share, are minimal internal
306 censoring artefacts (see supplemental material containing the original fracture maps), good
307 connectivity of fractures in terms of intersections with model boundaries (Figure 7), to ensure
308 that flow is characterised as part of a larger connected network, and an abundance of the N-S
309 and/or E-W trending fractures (Figure 3c). Each outcrop contains at least several hundred
310 fractures, and the spatial distribution varies strongly between outcrops and sometimes within
311 outcrops. The windows for each of the four outcrops that satisfy these criteria are illustrated
312 in Figure 7:

313 i) Apodi 2, which contains N-S, NE-SW and NW-SE striking fractures (Figure 7a);
314 ii) Apodi 3, with large partly intersecting fractures striking approximately NE-SW,
315 and smaller E-W striking fractures that are mostly limited to the SW part of the
316 outcrop (Figure 7b);

iii) Apodi 4, with an orthogonal fully percolating fracture system striking N-S and E-W (Figure 7c); and

iv) Dix-Sept 1, with scattered orientations where many small fractures are abutting against less intense, larger WNE-ESE fractures (Figure 7d).

The other outcrops contribute to our documentation that geometric variation is quite prevalent for fracture networks across the study area, but were not needed for the permeability modelling because these four outcrops served to show the variation while having some similarities for consideration.

4.1. Modelling methodology

Rather than conventional upscaling of geometry to effective flow properties, we model flow through a discrete network of fractures in a permeable matrix, based on the four outcrops (Figure 7). Flow is modelled in 2-D, representative of horizontal permeability between wells, as an analogue for production from a fractured reservoir. We consider single-phase flow, which is representative for early production from a hydrocarbon reservoir, but may not be applicable to secondary recovery methods (Gong and Rossen, 2016). The present surface fracture apertures are not representative of subsurface conditions because of stress-relief during exhumation and aperture enhancement due to recent weathering, hence we use a stress-sensitive aperture model based on estimated subsurface stress representative of pre-exhumation conditions for the conditions that we are modelling.

4.1.1. Aperture modelling

Some preserved veins are found in the Jandaíra Formation, which have shear and opening components (Figure 2b). Based on these observations, we model apertures as a function of stress using the Barton-Bandis model, which describes the opening of sheared fractures with irregular fracture walls (Barton, 1976; Barton and Bandis, 1980). It assumes that, in the

absence of high fluid pressures, fractures have an intrinsic roughness that prevents complete closing when some shear occurs, resulting in hydraulic apertures of up to 0.5 mm (Olsson and Barton, 2001; Barton, 2014). This aperture magnitude corresponds to the limited measurements of veins with matching boundaries made from thin sections (de Graaf et al., 2017).

Barton-Bandis aperture is a function of intrinsic fracture properties, predominantly the fracture roughness (Joint Roughness Coefficient JRC) and strength (Joint Compressive Strength JCS), and the local normal and shear stresses (Barton and Bandis, 1980). We use a constant JRC of 15, representative of somewhat irregular fracture walls corresponding to qualitative observations of veins in small preserved sections of outcrops, and a JCS of 120 MPa, representative of non-weathered surfaces. We approximate local normal and shear stresses using a method that does not require Finite Element modelling, but instead uses far-field stresses in combination with the local network geometry (Bisdom et al., 2016a). For all networks, constant stress boundary conditions and mechanical rock properties are used, with a horizontal maximum stress of 30 MPa, representative of stress conditions at depths of around 2.5 – 3 km in the Potiguar basin (Reis et al., 2013). For a fully elastic rock matrix with a Young's modulus of 50 GPa and a Poisson's ratio of 0.3, a Poisson's stress of 10 MPa is generated. The resulting ratio between shear displacement and normal stress then defines the hydraulic aperture (Olsson and Barton, 2001; Bisdom et al., 2016c). As the models are limited to 2-D horizontal sections, overburden stresses are not considered.

4.1.2. Permeability modelling

To model flow through the fracture network we generate a mesh that is conformable to a selected fracture geometry using ABAQUS® (Dassault Systèmes®). Each outcrop model is meshed with 2-D triangular elements representing the matrix and 1-D line elements representing fractures (Bisdom et al., 2016c). Intrinsic fracture permeability is calculated

from local apertures using the cubic law, assuming flow between parallel plates (Snow, 1969). To account for potential flow from disconnected fractures, we assume a constant matrix permeability of 1 mD, which is later increased to up to 100 mD to study the impact of matrix flow, and calculate along each fracture element the flow exchange between fracture and matrix.

Flow is modelled using the Complex Systems Modelling Platform (CSMP++; Matthäi et al., 2007), which models the fluid-pressure distribution for single-phase incompressible flow through fractures and matrix (e.g. Matthäi and Belayneh, 2004). A fluid pressure gradient is applied in the directions parallel to the model edges (e.g. E-W and N-S; Figure 8). This choice does not necessarily capture the maximum permeability, but our aim is to characterise relative permeability trends between different networks. From the fluid-pressure gradient, we derive the equivalent permeability in the two horizontal directions, which is the permeability representative of combined fracture and matrix flow within the model (Paluszny and Matthäi, 2010; Nick and Matthäi, 2011).

4.2. Results

4.2.1. Variability in inter-well scale permeability

For the applied boundary conditions and fracture properties, Barton-Bandis apertures range between 0-0.28 mm (Figure 7). The corresponding equivalent permeability in a 1 mD matrix is quantified as the ratio between equivalent permeability and matrix permeability in the E-W and N-S directions (Figure 9a). Except for Apodi 2, permeability is anisotropic and greatest in the N-S flow direction. Anisotropy is greatest in Apodi 3, which contains predominantly long N-S striking conjugates and joints. The limited number of E-W striking fracture traces in this outcrop have small lengths so E-W-directed connectivity is weak. Permeability is nearly isotropic in Apodi 4, which has an orthogonal system of N-S and E-W striking fractures with a homogeneous intensity, and Dix-Sept 1, which has a scattered orientation distribution with

no prominent modal orientations, resulting in the lack of a preferential flow direction. In Apodi 2, fewer fractures strike N-S compared to the other outcrops, resulting in a more isotropic permeability distribution.

The contribution of fracture flow to equivalent permeability, averaged over the two flow directions, ranges from 3.5 to 8, as compared to matrix flow (Figure 9b). We found no relation between geometry, specifically length and intensity, and permeability (Figure 9b). The outcrop with the greatest permeability does have the largest P_{21} intensity (Apodi 4), but a small average fracture length, whereas Apodi 3, which has a similar intensity and significantly larger average length, has the lowest permeability. Although particularly intensity is generally considered to determine permeability, we found no correlation between permeability and intensity for these networks in a 1 mD permeable matrix.

4.2.2. Percolation probability as a proxy for permeability

As permeability variations cannot be related to a single geometrical parameter, we compared the permeability results with the percolation probabilities, which encompass fracture count and connectivity, to assess whether percolation probability is a more representative proxy for permeability than intensity or length. In addition to the percolation probability defined by (Robinson, 1983, 1984), we consider a second definition, network saturation (Hürxkens, 2011). Network saturation is defined as the ratio between the area of the cluster and the total outcrop area, and ranges between 0-100%. Network saturation was calculated using FracMan® (Golder Associates®).

The percolation probability defined by Robinson (1983) has a positive correlation with permeability for three outcrops, although the correlation is not fully linear (Figure 10a). Moreover, percolation significantly underestimates the flow potential of Apodi 4. This method implicitly accounts for intensity, length and orientation, as a large scatter in

orientation and long fractures increase the probability of intersecting fractures. However, the intersection count can also be large when fractures are short and clustered, but if these fractures do not form a connecting network from one side of the model to the other boundary, permeability will be low even though the percolation probability is high.

Defining the percolation probability as network saturation improves the relation with equivalent permeability in a 1 mD matrix (Figure 10b). Contrary to the previous method, this method considers the spatial arrangement explicitly. However, since both methods assume that the matrix is impermeable, the correlation between connectivity and permeability does not hold for larger matrix permeabilities (Figure 10c,d). This outcome is further illustrated by outcrops Apodi 2 and Dix-Sept 1, which have similar network saturations and a similar equivalent permeability in a 1 mD matrix (Figure 10b), but permeability of the two networks differs noticeably when matrix permeability increases (Figure 10c,d).

5. Discussion

The large permeability variations between different outcrops that are only 300 m to several km apart, illustrate the impact of natural fracture variability on permeability (Figure 9a). Outcrops Apodi 3 and 4, which are less than 2 km apart, have the largest contrast in permeability, whereas the Dix-Sept 1 and Apodi 2 have comparable permeabilities although they are nearly 20 km apart. Equivalent permeability as a ratio of matrix permeability ranges from 3.5 to 8, which reflects the combined impact of orientation, intensity, length and connectivity, but cannot be related to any of these parameters individually, nor to definitions of percolation probability that consider multiple geometrical parameters (Figure 9b). Note that the aperture range predicted by Barton-Bandis is relatively narrow, and that the permeability contrasts between outcrops likely increases for other aperture definitions (Bisdom et al., 2016b).

Conventional DFN modelling based on 1-D geometry distributions cannot account for this intrinsic variability of geometry. Using a combination of representative power-law exponents for fracture length and the fractal dimension does introduce more variability into the system (Darcel, 2003), but most fracture datasets do not contain a sufficient number of fractures covering several orders of magnitude in length and intensity to usefully constrain these parameters. Even the dataset in this study, containing an average of nearly 1,500 fractures per outcrop, has sampling and truncation artefacts that limit the orders of magnitude of fracture length and intensity.

Instead of trying to capture multidimensional fracture patterns and their intrinsic variability in 1-D distributions that subsequently need to be extrapolated to 2-D or 3-D for DFN models, we propose to use a multiscale approach to capture fracture patterns in 2-D and directly use these deterministic patterns as input for flow models to better understand the impact of geometry variations on permeability, and to derive lessons for subsurface analogue reservoirs. The limitation that outcrops are not a direct proxy for flow is overcome by using a stress-sensitive aperture model representative of fractures in reservoirs with shear-induced fractures and low pore pressures, where Barton-Bandis is considered most representative.

The applied DFM flow modelling approach quantifies the uncertainty range in permeability associated with intrinsic network variability without a need for upscaling, but as this method is computationally expensive, its application is limited to relatively small-scale models (Geiger et al., 2010; Geiger and Matthäi, 2012). When matrix permeability is small or absent, geometry-based percolation methods can be a good proxy for permeability in reservoir-scale models, but they should ideally account for the 2-D or 3-D spatial distribution (e.g. de Dreuzy et al., 2000) rather than 1-D distributions. Individual geometrical parameters, such as P_{21} intensity, are insufficient as a proxy for permeability (Figure 9b).

6. Conclusion

The geometrical and flow analysis of the fracture patterns in the Potiguar basin illustrates the impact of natural variability of fractures on uncertainties in permeability. A scatter in geometry that is only partly related to seismic-scale deformation such as regional faults leads to significant variations in the equivalent permeability ratio, with a ratio between 3.5 and 8 in outcrops that are only several hundred metres to several kilometres apart from each other. In fractured reservoir models, these areas typically represent several upscaled grid cells in between wells. The effective fracture-flow properties of these cells are controlled by geometrical trends defined by seismic-scale folds or faults, but they rarely consider the intrinsic variability of fractures. Outcrop analogues do illustrate this variability, but most studied outcrops are too small to quantify this variability usefully for inclusion in models. The fracture patterns in the Potiguar basin are an excellent example of intrinsic variability of natural fracture patterns, providing sub-horizontal exposures of several hundred by several hundred metres where more than 13,000 of fractures were mapped.

Within each outcrop and between different outcrops, differences in intensity and length of barren fractures exist that cannot be related to the large-scale structural position of each outcrop in the basin. Conventional DFN modelling using 1-D probability distributions does not capture this scatter. To quantify the impact of intrinsic fracture geometry variations on reservoir permeability, we model the equivalent permeability in the digitised deterministic fracture networks using Discrete Fracture-Matrix (DFM) flow modelling, where fractures are represented as discrete features with a heterogeneous aperture distribution derived from geomechanical relations. These models consider that natural fractures have an intrinsic roughness that creates a hydraulic aperture even when fluid pressure is low, as long as fractures experienced some shear displacement.

We find that in between outcrops that are several hundred metres apart, a large scatter occurs in equivalent permeability and permeability anisotropy. The distance between these outcrops is comparable to well spacing in large fractured carbonate reservoirs in for example the Middle East, and the results illustrate that even in reservoirs with relatively little regional-scale deformation, fracture permeability varies greatly at an inter-well scale. Percolation probabilities record this scatter, but we find that percolation is only representative of permeability when fractures are the only features that contribute to permeability in a reservoir. Alternatively, defining permeability as an equivalent permeability that includes flow through fractures and matrix, as well as subseismic-scale variations in fracture geometry, the permeability of fractured reservoirs can be more accurately modelled at reservoir-scales, using conventional grid-based flow models.

Acknowledgements

Total S.A. is thanked for sponsoring the PhD of the first author. We thank the National Petroleum Agency (ANP) of Brazil, Petrobras (Porocarste Project) and the Brazilian Research Council (CNPq) project "The syn- to post-rift evolution of the NE Brazil passive continental margin: implication for sedimentary systems and deformation structures" (no. 406261/2013-0, PVE) for supporting the fieldwork. . Acquisition and interpretation of fracture data was partly done by Mariska van Eijk and Eva van der Voet (VU University Amsterdam) and Coen Paulides (Delft University of Technology), with additional support from numerous students and staff from the Federal University of Rio Grande Do Norte (UFRN) in Brazil. We thank Hamidreza M. Nick (now at the Technical University of Denmark) for his support with the flow simulations. We acknowledge Golder Associates for supplying licenses and support for FracMan. The initial manuscript has been significantly improved thanks to constructive reviews by Clare Bond, Aisling Soden, and the Editor (William Dunne).

References

Assumpção, M., 1992, The regional intraplate stress field in South America: Journal of Geophysical Research, v. 97, no. B8, p. 11889, doi:10.1029/91JB01590.

Barton, N., 2014, Non-linear behaviour for naturally fractured carbonates and frac-stimulated gas-shales: First Break, v. 32, no. 2031, p. 51–66, doi:10.3997/1365-2397.2014011.

Barton, N., 1976, The shear strength of rock and rock joints: International Journal of Rock Mechanics and Mining Sciences & Geomechanics Abstracts, v. 13, no. 9, p. 255–279, doi:10.1016/0148-9062(76)90003-6.

Barton, N., and S. Bandis, 1980, Some effects of scale on the shear strength of joints, *in* International Journal of Rock Mechanics and Mining Sciences & Geomechanics Abstracts: Pergamon Press Ltd., p. 69–73, doi:http://dx.doi.org/10.1016/0148-9062(80)90009-1.

Belayneh, M., and J. W. Cosgrove, 2010, Hybrid veins from the southern margin of the Bristol Channel Basin, UK: Journal of Structural Geology, v. 32, no. 2, p. 192–201, doi:10.1016/j.jsg.2009.11.010.

Belayneh, M. W., S. K. Matthäi, M. J. Blunt, and S. F. Rogers, 2009, Comparison of deterministic with stochastic fracture models in water-flooding numerical simulations: AAPG Bulletin, v. 93, no. 11, p. 1633–1648, doi:10.1306/07220909031.

Bergbauer, S., 2007, Testing the predictive capability of curvature analyses: Geological Society, London, Special Publications, v. 292, no. 1, p. 185–202, doi:10.1144/SP292.11.

Berkowitz, B., 1995, Analysis of fracture network connectivity using percolation theory: Mathematical Geology, v. 27, no. 4, p. 467–483, doi:10.1007/BF02084422.

Berkowitz, B., 2002, Characterizing flow and transport in fractured geological media: A review: Advances in Water Resources, v. 25, no. 8–12, p. 861–884, doi:10.1016/s0309-1708(02)00042-8.

Berkowitz, B., and I. Balberg, 1993, Percolation theory and its application to groundwater hydrology: Water Resour. Res., v. 29, no. 4, p. 775–794, doi:10.1029/92wr02707.

Bezerra, F. H. R., M. K. Takeya, M. O. L. Sousa, and A. F. do Nascimento, 2007, Coseismic reactivation of the Samambaia fault, Brazil: Tectonophysics, v. 430, no. 1–4, p. 27–39, doi:10.1016/j.tecto.2006.10.007.

Bezerra, F. H. R., and C. Vita-Finzi, 2000, How active is a passive margin? Paleoseismicity in northeastern Brazil: Geology, v. 28, no. 7, p. 591, doi:10.1130/0091-7613(2000)28<591:HAIAPM>2.0.CO;2.

Bisdom, K., G. Bertotti, and H. M. Nick, 2016a, A geometrically based method for predicting stress-induced fracture aperture and flow in discrete fracture networks: AAPG Bulletin, v. 100, no. 7, p. 1075–1097, doi:10.1306/02111615127.

Bisdom, K., G. Bertotti, and H. M. Nick, 2016b, The impact of different aperture distribution models and critical stress criteria on equivalent permeability in fractured rocks: Journal of Geophysical Research: Solid Earth, v. 121, no. 5, p. 4045–4063, doi:10.1002/2015JB012657.

Bisdom, K., G. Bertotti, and H. M. Nick, 2016c, The impact of in-situ stress and outcrop-based fracture geometry on hydraulic aperture and upscaled permeability in fractured reservoirs: Tectonophysics, v. 690, p. 63–75, doi:10.1016/j.tecto.2016.04.006.

Bisdom, K., B. D. M. Gauthier, G. Bertotti, and N. J. Hardebol, 2014, Calibrating discrete fracture-network models with a carbonate three-dimensional outcrop fracture network: Implications for naturally fractured reservoir modeling: AAPG Bulletin, v. 98, no. 7, p. 1351–1376, doi:10.1306/02031413060.

Bond, C. E., R. Wightman, and P. S. Ringrose, 2013, The influence of fracture anisotropy on

560 CO2 flow: Geophysical Research Letters, v. 40, no. 7, p. 1284–1289,
561 doi:10.1002/grl.50313.
562 Bonneau, F., G. Caumon, and P. Renard, 2016, Impact of a Stochastic Sequential Initiation of
563 Fractures on the Spatial Correlations and Connectivity of Discrete Fracture Networks:
564 Journal of Geophysical Research: Solid Earth, p. 1–18, doi:10.1002/2015JB012451.
565 Bonnet, E., O. Bour, N. E. Odling, P. Davy, I. Main, P. Cowie, and B. Berkowitz, 2001,
566 Scaling of fracture systems in geological media: Reviews of Geophysics, v. 39, no. 3, p.
567 347–383, doi:10.1029/1999RG000074.
568 Bourbiaux, B., R. Basquet, M.-C. Cacas, J.-M. Daniel, and S. Sarda, 2002, An Integrated
569 Workflow to Account for Multi-Scale Fractures in Reservoir Simulation Models:
570 Implementation and Benefits, *in* Proceedings of Abu Dhabi International Petroleum
571 Exhibition and Conference: Society of Petroleum Engineers, doi:10.2118/78489-MS.
572 Brito Neves, B. B. de, R. A. Fuck, U. G. Cordani, and A. Thomaz F, 1984, Influence of
573 basement structures on the evolution of the major sedimentary basins of Brazil: A case
574 of tectonic heritage: Journal of Geodynamics, v. 1, no. 3–5, p. 495–510,
575 doi:10.1016/0264-3707(84)90021-8.
576 Cosgrove, J. W., 2001, Hydraulic fracturing during the formation and deformation of a basin:
577 A factor in the dewatering of low-permiability sediments: AAPG Bulletin, v. 85, no. 4,
578 p. 737–748, doi:10.1306/8626C997-173B-11D7-8645000102C1865D.
579 Darcel, C., 2003, Stereological analysis of fractal fracture networks: Journal of Geophysical
580 Research, v. 108, no. B9, p. 2451, doi:10.1029/2002JB002091.
581 Dershowitz, W. S., and H. H. Einstein, 1988, Characterizing rock joint geometry with joint
582 system models: Rock Mechanics and Rock Engineering, v. 51, no. 1, p. 21–51,
583 doi:10.1007/bf01019674.
584 de Dreuzy, J.-R., P. Davy, and O. Bour, 2002, Hydraulic properties of two-dimensional
585 random fracture networks following power law distributions of length and aperture:
586 Water Resources Research, v. 38, no. 12, p. 12-1-12–9, doi:10.1029/2001WR001009.
587 de Dreuzy, J.-R., P. Davy, and O. Bour, 2000, Percolation parameter and percolation-
588 threshold estimates for three-dimensional random ellipses with widely scattered
589 distributions of eccentricity and size: Physical Review E, v. 62, no. 5, p. 5948–5952,
590 doi:10.1103/PhysRevE.62.5948.
591 Ebner, M., D. Koehn, R. Toussaint, F. Renard, and J. Schmittbuhl, 2009, Stress sensitivity of
592 stylolite morphology: Earth and Planetary Science Letters, v. 277, no. 3–4, p. 394–398,
593 doi:10.1016/j.epsl.2008.11.001.
594 Fernandes, A. L., W. E. Medeiros, F. H. R. Bezerra, J. G. Oliveira, and C. L. Cazarin, 2015,
595 GPR investigation of karst guided by comparison with outcrop and unmanned aerial
596 vehicle imagery: Journal of Applied Geophysics, v. 112, p. 268–278,
597 doi:10.1016/j.jappgeo.2014.11.017.
598 Follin, S., L. Hartley, I. Rhén, P. Jackson, S. Joyce, D. Roberts, and B. Swift, 2014, A
599 methodology to constrain the parameters of a hydrogeological discrete fracture network
600 model for sparsely fractured crystalline rock, exemplified by data from the proposed
601 high-level nuclear waste repository site at Forsmark, Sweden: Hydrogeology Journal, v.
602 22, p. 313–331, doi:10.1007/s10040-013-1080-2.
603 Gauthier, B. D. M., M. Garcia, J.-M. J. Daniel, A. M. Zellou, A. Toublanc, M. Garcia, and J.-
604 M. J. Daniel, 2002, Integrated Fractured Reservoir Characterization: A Case Study in a
605 North Africa Field: SPE Reservoir Evaluation & Engineering, v. 5, no. 4, p. 24–25,
606 doi:10.2118/79105-PA.
607 Geiger, S., A. Cortis, and J. T. Birkholzer, 2010, Upscaling solute transport in naturally
608 fractured porous media with the continuous time random walk method: Water Resources
609 Research, v. 46, no. 12, doi:10.1029/2010WR009133.

610 Geiger, S., and S. Matthäi, 2012, What can we learn from high-resolution numerical
611 simulations of single- and multi-phase fluid flow in fractured outcrop analogues?
612 Geological Society, London, Special Publications, v. 374, no. 1, p. 125–144,
613 doi:10.1144/SP374.8.
614 Gillespie, P. ., J. . Walsh, J. Watterson, C. . Bonson, and T. Manzocchi, 2001, Scaling
615 relationships of joint and vein arrays from The Burren, Co. Clare, Ireland: Journal of
616 Structural Geology, v. 23, no. 2–3, p. 183–201, doi:10.1016/S0191-8141(00)00090-0.
617 Gong, J., and W. R. Rossen, 2016, Shape factor for dual-permeability fractured reservoir
618 simulation: Effect of non-uniform flow in 2D fracture network: Fuel, v. 184, p. 81–88,
619 doi:10.1016/j.fuel.2016.06.113.
620 de Graaf, S., J. J. G. Reijmer, G. V. Bertotti, F. H. R. Bezerra, C. L. Cazarin, K. Bisdom, and
621 H. B. Vonhof, 2017, Fracturing and calcite cementation controlling fluid flow in the
622 shallow-water carbonates of the Jandaíra Formation, Brazil: Marine and Petroleum
623 Geology, v. 80, p. 382–393, doi:10.1016/j.marpetgeo.2016.12.014.
624 Gurgel, S. P. P., F. H. R. Bezerra, A. C. B. Corrêa, F. O. Marques, and R. P. Maia, 2013,
625 Cenozoic uplift and erosion of structural landforms in NE Brazil: Geomorphology, v.
626 186, p. 68–84, doi:10.1016/j.geomorph.2012.12.023.
627 Hardebol, N. J., and G. Bertotti, 2013, DigiFract: A software and data model implementation
628 for flexible acquisition and processing of fracture data from outcrops: Computers &
629 Geosciences, v. 54, p. 326–336, doi:10.1016/j.cageo.2012.10.021.
630 Hardebol, N. J., C. Maier, H. Nick, S. Geiger, G. Bertotti, and H. Boro, 2015, Multiscale
631 fracture network characterization and impact on flow: A case study on the Latemar
632 carbonate platform: Journal of Geophysical Research: Solid Earth, v. 120, no. 12, p.
633 8197–8222, doi:10.1002/2015JB011879.
634 Hodgetts, D., 2013, Laser scanning and digital outcrop geology in the petroleum industry: A
635 review: Marine and Petroleum Geology, v. 46, p. 335–354,
636 doi:10.1016/j.marpetgeo.2013.02.014.
637 Hürxkens, C. C. M. J., 2011, The Sensitivity of the 3D Connectivity in a Multi-Scale Fracture
638 Network to Variations in Distribution Parameters: A Case Study from Petra, Jordan:
639 Delft University of Technology, 46 p.
640 Jones, R. J., 1965, Aspects of the biological weathering of Limestone pavement: Proceedings
641 of the Geologists' Association, v. 76, no. 4, p. 421–IN8, doi:10.1016/S0016-
642 7878(65)80041-4.
643 Kemeny, J., and R. Post, 2003, Estimating three-dimensional rock discontinuity orientation
644 from digital images of fracture traces: Computers & Geosciences, v. 29, no. 1, p. 65–77,
645 doi:10.1016/S0098-3004(02)00106-1.
646 Kirkpatrick, J. D., F. H. R. Bezerra, Z. K. Shipton, A. F. Do Nascimento, S. I. Pytharouli, R.
647 J. Lunn, and A. M. Soden, 2013, Scale-dependent influence of pre-existing basement
648 shear zones on rift faulting: a case study from NE Brazil: Journal of the Geological
649 Society, v. 170, no. 2, p. 237–247, doi:10.1144/jgs2012-043.
650 Laurich, B., J. L. Urai, G. Desbois, C. Vollmer, and C. Nussbaum, 2014, Microstructural
651 evolution of an incipient fault zone in Opalinus Clay: Insights from an optical and
652 electron microscopic study of ion-beam polished samples from the Main Fault in the Mt-
653 Terri Underground Research Laboratory: Journal of Structural Geology, v. 67, no. PA,
654 p. 107–128, doi:10.1016/j.jsg.2014.07.014.
655 Lei, Q., and X. Wang, 2016, Tectonic interpretation of the connectivity of a multiscale
656 fracture system in limestone: Geophysical Research Letters, v. 43, no. 4, p. 1551–1558,
657 doi:10.1002/2015GL067277.
658 Long, J. C. S., and D. M. Billaux, 1987, From field data to fracture network modeling: An
659 example incorporating spatial structure: Water Resources Research, v. 23, no. 7, p.

660 1201–1216, doi:10.1029/WR023i007p01201.
661 Makel, G. H., 2007, The modelling of fractured reservoirs: constraints and potential for
662 fracture network geometry and hydraulics analysis: Geological Society, London, Special
663 Publications, v. 292, no. 1, p. 375–403, doi:10.1144/SP292.21.
664 Matos, R. M. D. de, 1992, The Northeast Brazilian Rift System: Tectonics, v. 11, no. 4, p.
665 766–791, doi:10.1029/91TC03092.
666 Matthäi, S. K. et al., 2007, Numerical simulation of multi-phase fluid flow in structurally
667 complex reservoirs: Geological Society, London, Special Publications, v. 292, no. 1, p.
668 405–429, doi:10.1144/SP292.22.
669 Matthäi, S. K., and M. Belayneh, 2004, Fluid flow partitioning between fractures and a
670 permeable rock matrix: Geophysical Research Letters, v. 31, no. 7,
671 doi:10.1029/2003GL019027.
672 Matthäi, S. K., and H. M. Nick, 2009, Upscaling two-phase flow in naturally fractured
673 reservoirs: AAPG Bulletin, v. 93, no. 11, p. 1621–1632, doi:10.1306/08030909085.
674 Nick, H. M., and S. K. Matthäi, 2011, Comparison of Three FE-FV Numerical Schemes for
675 Single- and Two-Phase Flow Simulation of Fractured Porous Media: Transport in
676 Porous Media, v. 90, no. 2, p. 421–444, doi:10.1007/s11242-011-9793-y.
677 Nick, H. M., A. Paluszny, M. J. Blunt, and S. K. Matthai, 2011, Role of geomechanically
678 grown fractures on dispersive transport in heterogeneous geological formations:
679 Physical Review E, v. 84, no. 5, p. 56301, doi:10.1103/PhysRevE.84.056301.
680 Nussbaum, C., P. Bossart, F. Amann, and C. Aubourg, 2011, Analysis of tectonic structures
681 and excavation induced fractures in the Opalinus Clay, Mont Terri underground rock
682 laboratory (Switzerland): Swiss Journal of Geosciences, v. 104, no. 2, p. 187–210,
683 doi:10.1007/s00015-011-0070-4.
684 Oda, M., 1985, Permeability tensor for discontinuous rock masses: Géotechnique, v. 35, no.
685 4, p. 483–495.
686 Odling, N., 1997, Scaling and connectivity of joint systems in sandstones from western
687 Norway: Journal of Structural Geology, v. 19, no. 10, p. 1257–1271, doi:10.1016/s0191-
688 8141(97)00041-2.
689 Odling, N. E., 2001, The scaling of hydraulic conductivity in rock fracture zones:
690 Geophysical Research Letters, v. 28, no. 15, p. 3019–3022, doi:10.1029/2000GL011863.
691 Odling, N. E. et al., 1999, Variations in fracture system geometry and their implications for
692 fluid flow in fractures hydrocarbon reservoirs: Petroleum Geoscience, v. 5, no. 4, p.
693 373–384, doi:10.1144/petgeo.5.4.373.
694 Odling, N. E., and J. E. Roden, 1997, Contaminant transport in fractured rocks with
695 significant matrix permeability, using natural fracture geometries: Journal of
696 Contaminant Hydrology, v. 27, no. 3–4, p. 263–283, doi:10.1016/S0169-
697 7722(96)00096-4.
698 Ojeda, H. A. O., 1982, Structural Framework, Stratigraphy, and Evolution of Brazilian
699 Marginal Basins: AAPG Bulletin, v. 66, no. 6, p. 732–749, doi:10.1306/03B5A309-
700 16D1-11D7-8645000102C1865D.
701 Olsson, R., and N. Barton, 2001, An improved model for hydromechanical coupling during
702 shearing of rock joints: International Journal of Rock Mechanics and Mining Sciences,
703 v. 38, no. 3, p. 317–329, doi:10.1016/S1365-1609(00)00079-4.
704 Ortega, O. J., R. A. Marrett, and S. E. Laubach, 2006, A scale-independent approach to
705 fracture intensity and average spacing measurement: AAPG Bulletin, v. 90, no. 2, p.
706 193–208, doi:10.1306/08250505059.
707 Paluszny, A., and S. K. Matthäi, 2010, Impact of fracture development on the effective
708 permeability of porous rocks as determined by 2-D discrete fracture growth modeling:
709 Journal of Geophysical Research, v. 115, no. B2, p. B02203,

710 doi:10.1029/2008JB006236.
711 Peacock, D. C. P., 2006, Predicting variability in joint frequencies from boreholes: Journal of
712 Structural Geology, v. 28, no. 2, p. 353–361, doi:10.1016/j.jsg.2005.10.007.
713 La Pointe, P. R., 1988, A method to characterize fracture density and connectivity through
714 fractal geometry: International Journal of Rock Mechanics and Mining Sciences &
715 Geomechanics Abstracts, v. 25, no. 6, p. 421–429, doi:10.1016/0148-9062(88)90982-5.
716 Price, N. J., 1966, Fault and Joint Development in Brittle and Semi-Brittle Rock: Pergamon,
717 192 p.
718 Reis, Á. F. C., F. H. R. Bezerra, J. M. Ferreira, A. F. Do Nascimento, and C. C. Lima, 2013,
719 Stress magnitude and orientation in the Potiguar Basin, Brazil: Implications on faulting
720 style and reactivation: Journal of Geophysical Research: Solid Earth, v. 118, no. 10, p.
721 5550–5563, doi:10.1002/2012JB009953.
722 Robinson, P. C., 1983, Connectivity of fracture systems-a percolation theory approach:
723 Journal of Physics A: Mathematical and General, v. 16, no. 3, p. 605–614,
724 doi:10.1088/0305-4470/16/3/020.
725 Robinson, P. C., 1984, Numerical calculations of critical densities for lines and planes:
726 Journal of Physics A: Mathematical and General, v. 17, no. 14, p. 2823–2830,
727 doi:10.1088/0305-4470/17/14/025.
728 Sanders, C., M. Bonora, D. Richards, E. Kozlowski, C. Sylwan, and M. Cohen, 2004,
729 Kinematic structural restorations and discrete fracture modeling of a thrust trap: a case
730 study from the Tarija Basin, Argentina: Marine and Petroleum Geology, v. 21, no. 7, p.
731 845–855, doi:10.1016/j.marpetgeo.2003.09.006.
732 Santos Filho, M. A. B. Dos, E. K. Piovesan, G. Fauth, and N. K. Srivastava, 2015,
733 Paleoenvironmental interpretation through the analysis of ostracodes and carbonate
734 microfacies: study of the Jandaíra Formation, Upper Cretaceous, Potiguar Basin:
735 Brazilian Journal of Geology, v. 45, no. 1, p. 23–34,
736 doi:10.1590/23174889201500010002.
737 Shackleton, J. R., M. L. Cooke, G. Seed, and A. D. Gibbs, 2009, Three-dimensional
738 modelling of Sant Corneli Anticline (Spain) using a hybrid-geometric/geomechanical
739 approach, *in* AAPG Annual Convention and Exhibition: AAPG.
740 Shackleton, J. R., M. L. Cooke, J. Vergés, and T. Simó, 2011, Temporal constraints on
741 fracturing associated with fault-related folding at Sant Corneli anticline, Spanish
742 Pyrenees: Journal of Structural Geology, v. 33, no. 1, p. 5–19,
743 doi:10.1016/j.jsg.2010.11.003.
744 Smart, K. J., D. a. Ferrill, and A. P. Morris, 2009, Impact of interlayer slip on fracture
745 prediction from geomechanical models of fault-related folds: AAPG Bulletin, v. 93, no.
746 11, p. 1447–1458, doi:10.1306/05110909034.
747 Snow, D. T., 1969, Anisotropic Permeability of Fractured Media: Water Resources Research,
748 v. 5, no. 6, p. 1273–1289, doi:10.1029/WR005i006p01273.
749 Soden, A. M., Z. K. Shipton, R. J. Lunn, S. I. Pytharouli, J. D. Kirkpatrick, A. F. Do
750 Nascimento, and F. H. R. Bezerra, 2014, Brittle structures focused on subtle crustal
751 heterogeneities: implications for flow in fractured rocks: Journal of the Geological
752 Society, v. 171, no. 4, p. 509–524, doi:10.1144/jgs2013-051.
753 Ukar, E., C. Ozkul, and P. Eichhubl, 2016, Fracture abundance and strain in folded Cardium
754 Formation, Red Deer River anticline, Alberta Foothills, Canada: Marine and Petroleum
755 Geology, v. 76, p. 210–230, doi:10.1016/j.marpetgeo.2016.05.016.
756 Vasuki, Y., E.-J. Holden, P. Kovesi, and S. Micklethwaite, 2014, Semi-automatic mapping of
757 geological Structures using UAV-based photogrammetric data: An image analysis
758 approach: Computers & Geosciences, v. 69, p. 22–32, doi:10.1016/j.cageo.2014.04.012.
759 Walsh, J. J., and J. Watterson, 1993, Fractal analysis of fracture patterns using the standard

box-counting technique: valid and invalid methodologies: Journal of Structural Geology, v. 15, no. 12, p. 1509–1512, doi:http://dx.doi.org/10.1016/0191-8141(93)90010-8.

Watkins, H., R. W. H. Butler, C. E. Bond, and D. Healy, 2015, Influence of structural position on fracture networks in the Torridon Group, Achnashellach fold and thrust belt, NW Scotland: Journal of Structural Geology, v. 74, p. 64–80, doi:10.1016/j.jsg.2015.03.001.

Wu, H. Q., and D. D. Pollard, 2002, Imaging 3-D fracture networks around boreholes: AAPG Bulletin, v. 86, no. 4, p. 593–604, doi:10.1306/61EEDB52-173E-11D7-8645000102C1865D.

Tables

Table 1 Summary of the average geometrical parameters (strike, length, intensity and percolation probability) for each outcrop.

	Orientation (strike) [°]	Length [m]	Intensity [m^{-1}]	Percolation probability [-]
Apodi 1	94	17.4	0.17	1.7
Apodi 2	81	16.6	0.17	2.0
Apodi 3	121	20.0	0.20	0.9
Apodi 4	82	7.1	0.21	1.5
Apodi 5	86	5.7	0.06	2.4
Dix-sept 1	81	5.5	0.31	1.7
Dix-sept 2	63	6.8	0.16	0.8
Mossoro 1	86	3.5	0.13	1.0
Mossoro 2	164	3.6	0.16	0.8

Figures

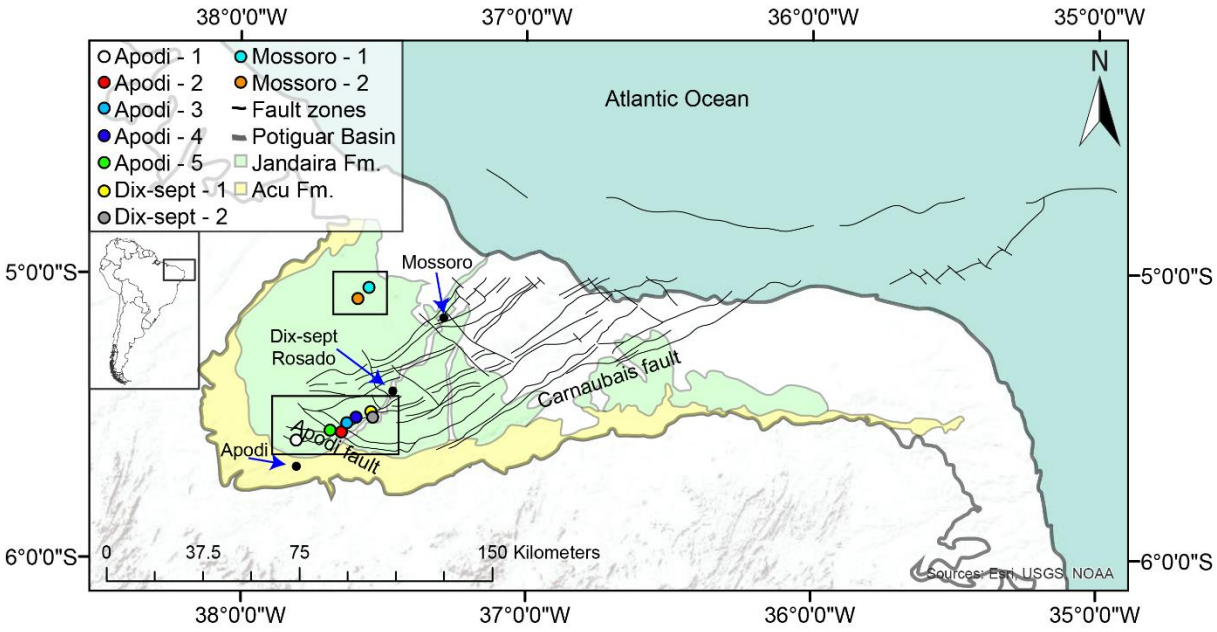

Figure 1 The Potiguar basin, containing NE-SW and NW-SE faults that are part of a graben system. The coloured areas indicate where the Jandaíra and Açu Formations outcrop. Coloured dots are locations for sampled fracture networks.

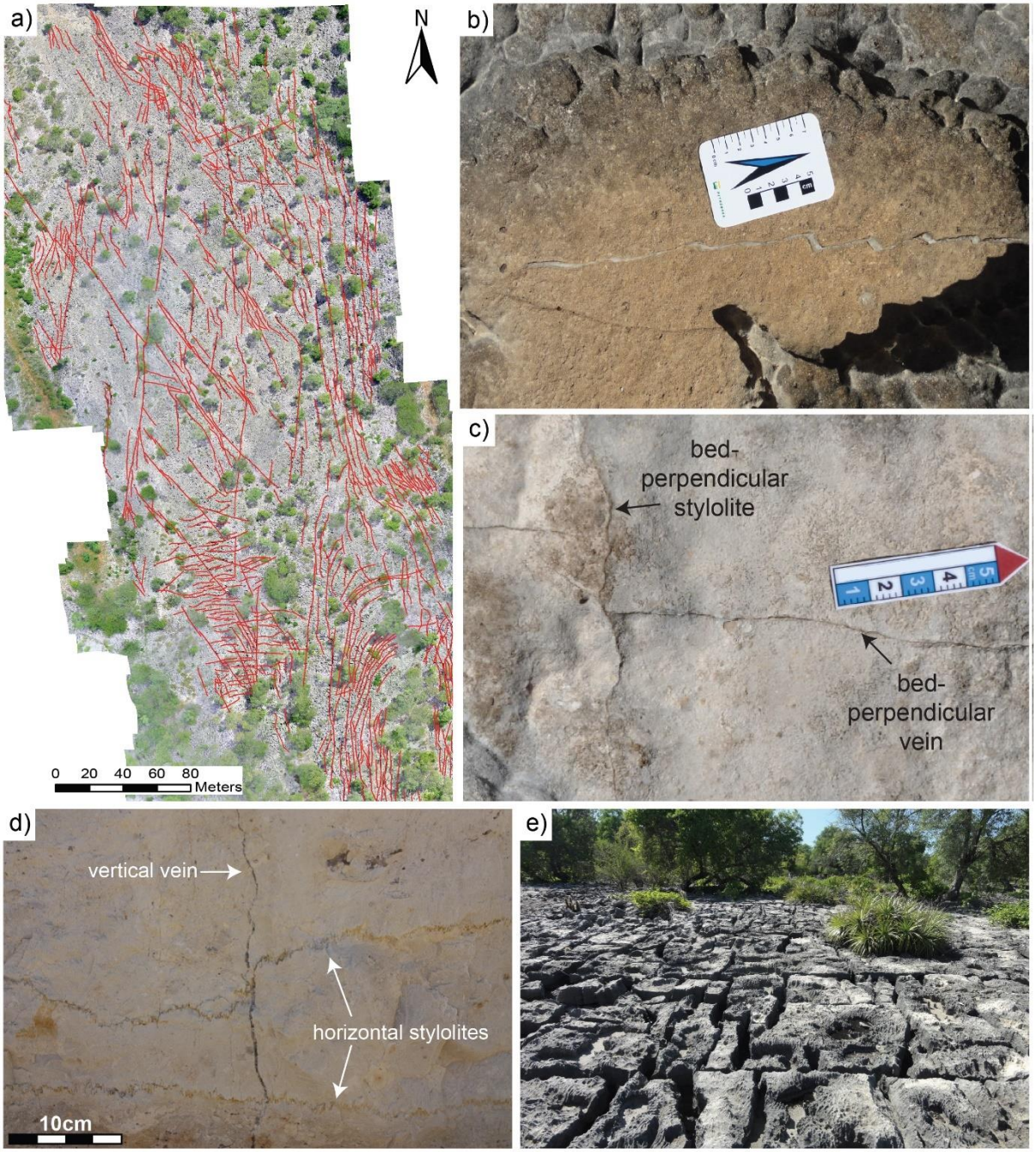

780

781 *Figure 2 Fracturing in the Jandaíra Fm.: a) Example of large-scale network digitised from*
782 *UAV imagery (Apodi 3); b) N-S striking bed-perpendicular vein with opening and shear*
783 *mode components; c) Top view of a detail from Apodi 4 showing a N-S striking bed-*
784 *perpendicular vein that is displaced by an E-W striking bed-perpendicular tectonic stylolite;*
785 *d) Vertical section showing a vertical vein that is cut by two horizontal stylolites; e) Detail of*
786 *Apodi 4, with dm-scale apertures related to clints and grikes.*

787 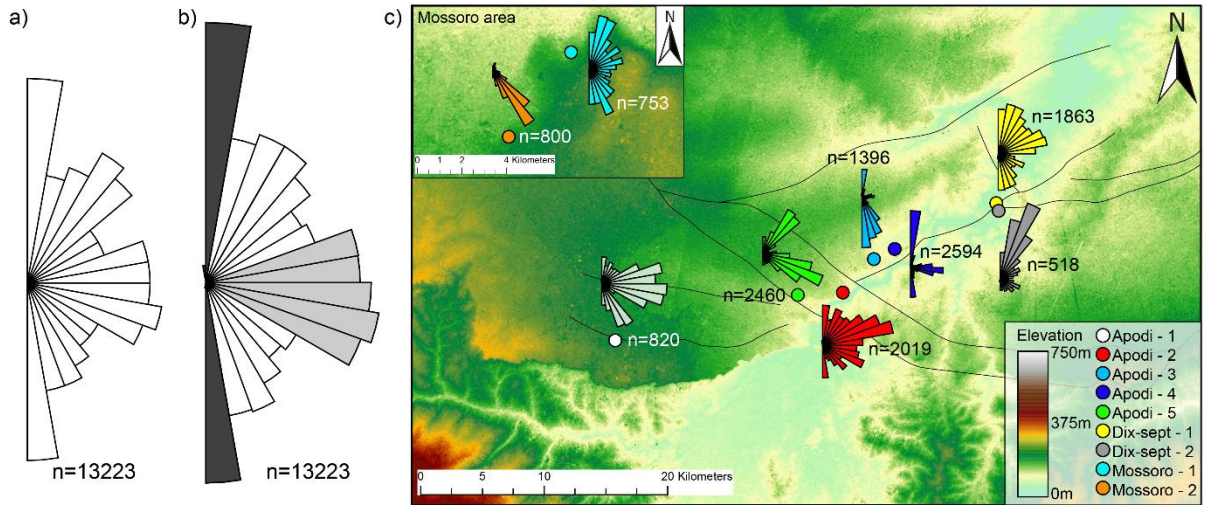

788 *Figure 3 Orientation distribution of barren fractures: a) Rose diagram of all 13,223 barren*
789 *fractures digitised in ten outcrops; b) Length-weighted rose diagram showing the*
790 *contribution of the two main N-S and E-W striking orientation trends to the length-weighted*
791 *distributions; c) False-colour map of a detail of the basin, showing the Apodi and Dix-Sept*
792 *outcrops, with the Mossoró outcrops in the top left inset. Regional faults indicated in black.*
793 *For each outcrop, the fracture orientations are shown in length-weighted rose diagrams,*
794 *with the number of digitised fractures.*

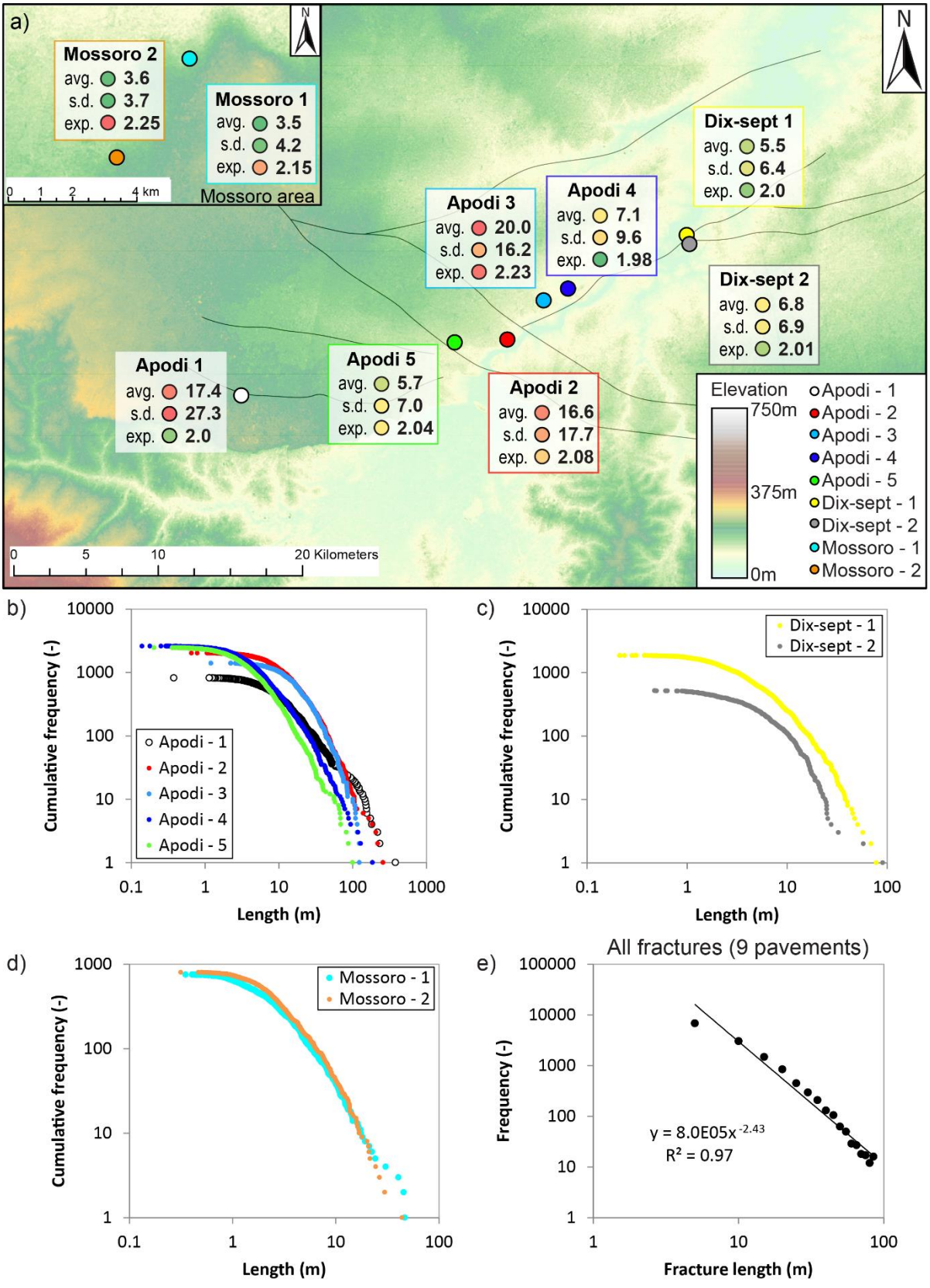

795

796 *Figure 4 Analysis of fracture length: a) Spatial variations in length attributes (average*

797 *length, standard deviation, and the power-law scaling exponent) in the individual outcrops,*

where the bar plots indicate relative trends in between the outcrops; b) Cumulative frequency distributions for the Apodi outcrops; c) Cumulative frequency for the Dix-Sept outcrops; d) Cumulative frequency for the Mosorro outcrops; e) Combined frequency distribution for fractures from all outcrops.

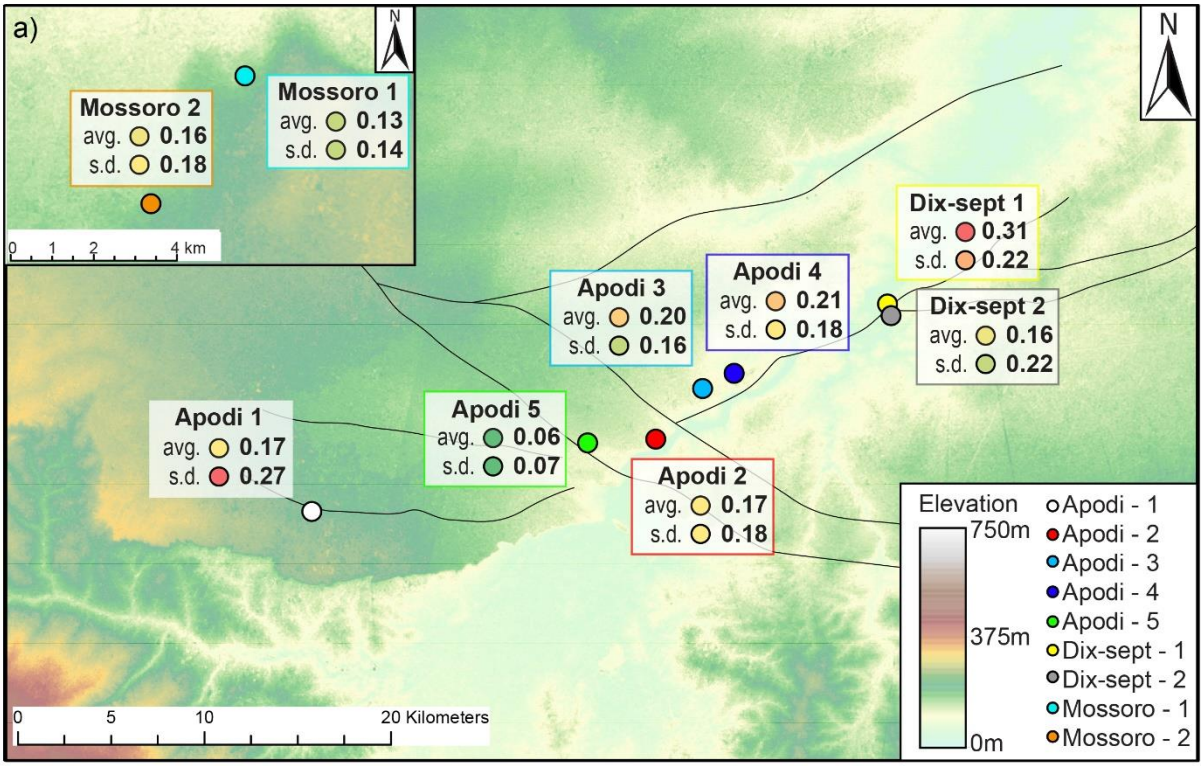

Figure 5 Spatial variations in P_{21} intensity attributes (average and standard deviation).

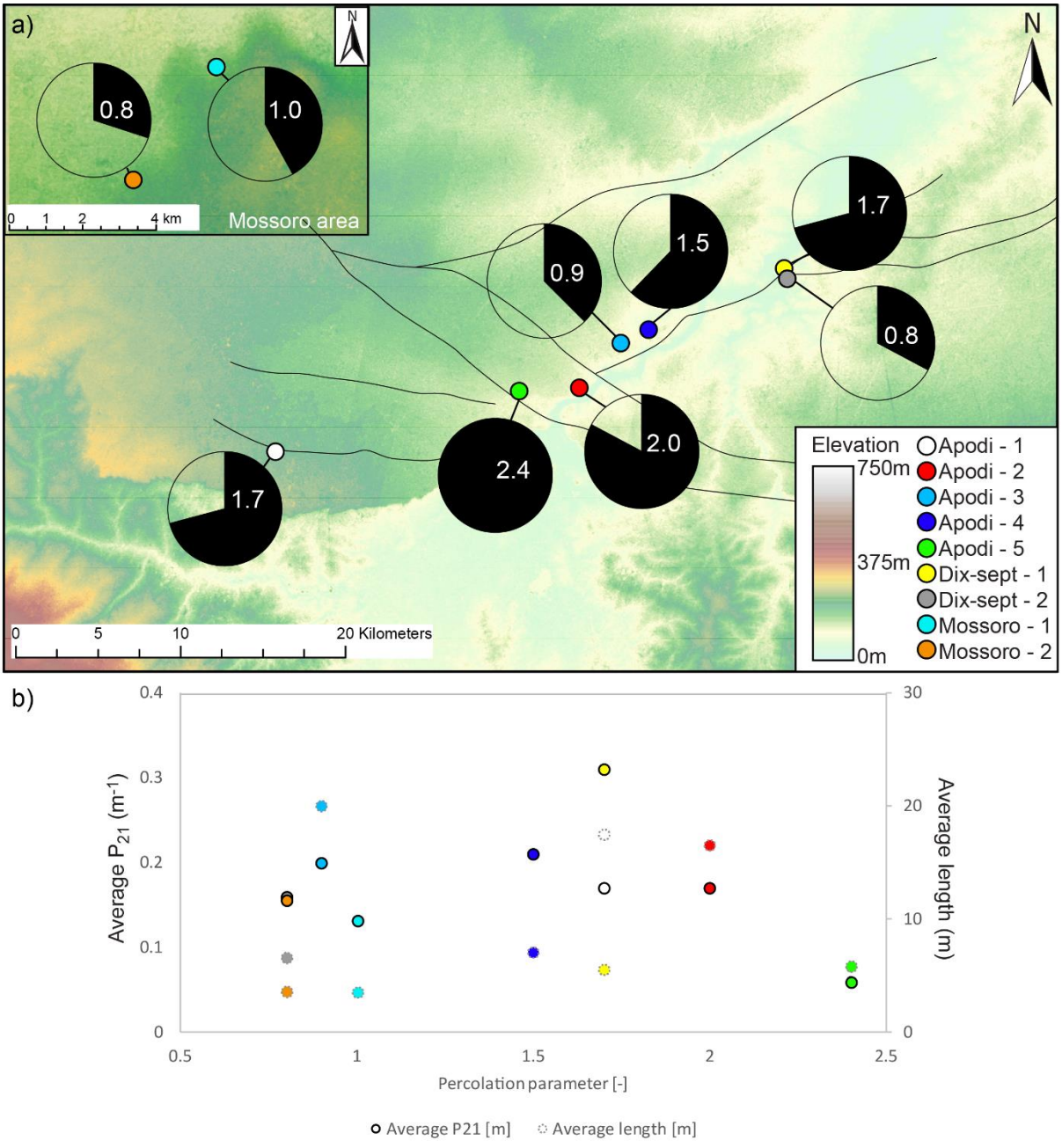

804

805 *Figure 6 Percolation parameters (intersections versus fracture count) for all outcrops: a)*
806 *The normalised percolation probability stated in each pie chart.; b) Percolation probability*
807 *versus average P_{21} (left vertical axis, circular symbols have solid black border) and average*
808 *length (right axis, circular symbols have dashed grey border) for all outcrops. Colour coding*
809 *of symbols corresponds to outcrop colours in (a).*

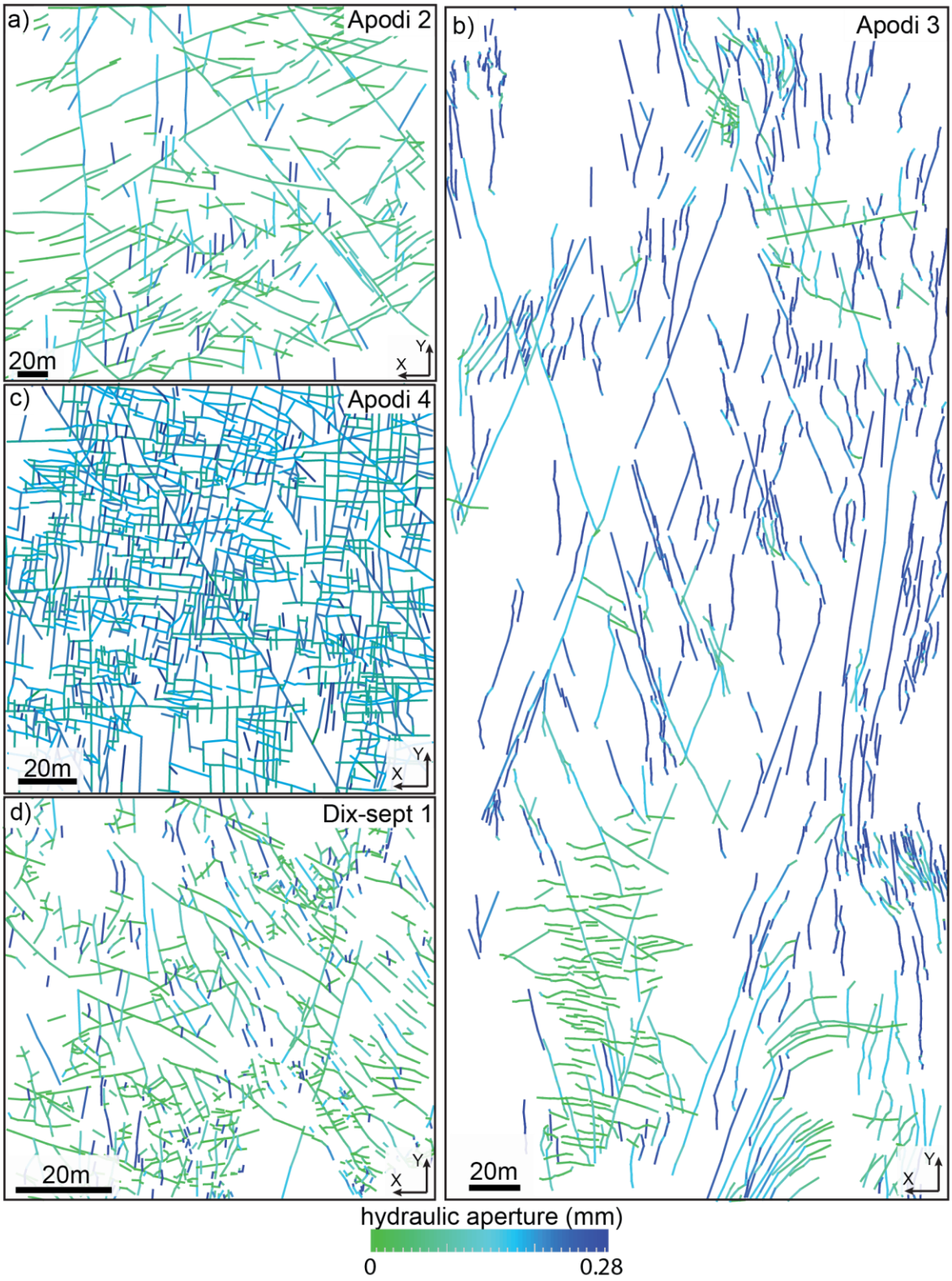

Figure 7 The hydraulic aperture distribution calculated using the Barton-Bandis shear aperture model, applied to the exhumed fracture networks of: a) Apodi 2; b) Apodi 3; c) Apodi 4; d) Dix-Sept 1. Adapted from (Bisdom et al., 2016b). *The colour range represents the*

hydraulic aperture calculated for the stress boundary conditions and rock properties used in this study.

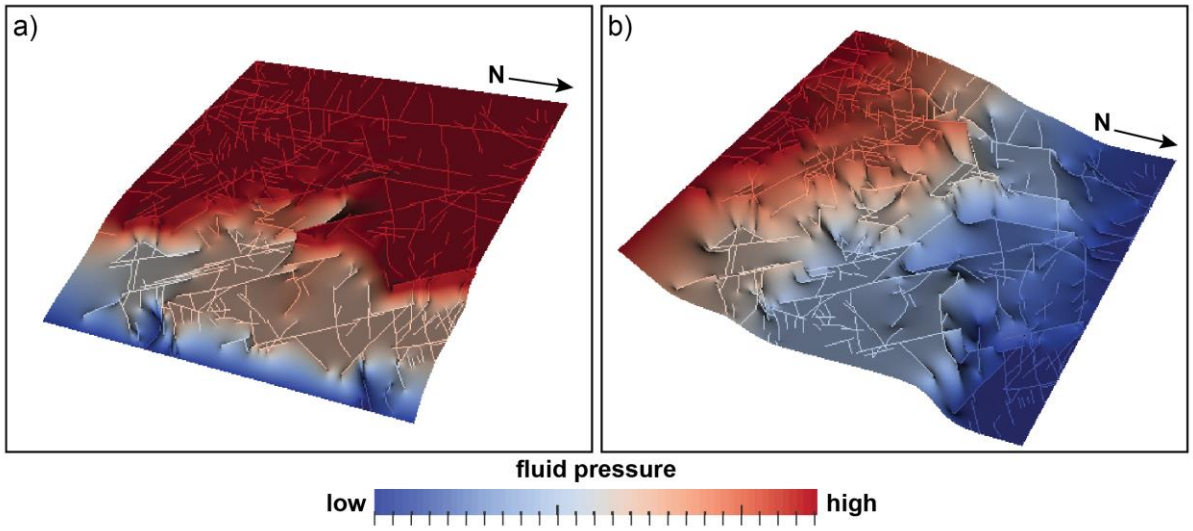

Figure 8 Fluid pressure distributions for Apodi 2 with a 1 mD matrix permeability and fracture permeability derived from the aperture distribution in Figure 7a: a) E-W fluid pressure; b) N-S fluid pressure.

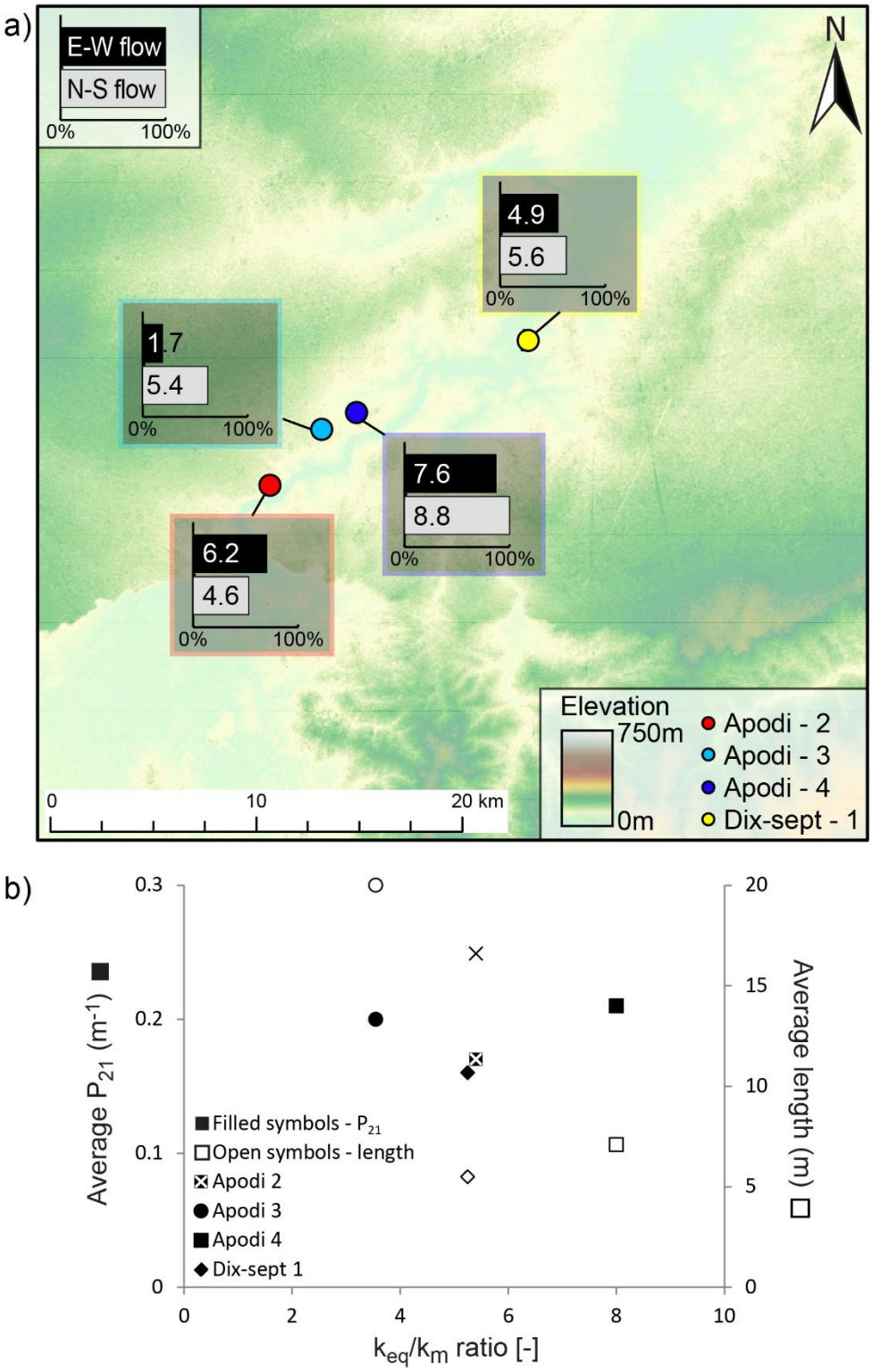

820

821 *Figure 9 a) Ratio between equivalent permeability and matrix permeability in the E-W and*
822 *N-S directions for four outcrops with barren fractures. The bar plots show the relative*
823 *differences in different outcrops and different directions, normalised for the largest*

permeability; b) Relation between the permeability ratio for each outcrop (average of the two directions) and average length (open symbols) and P_{21} intensity (filled symbols).

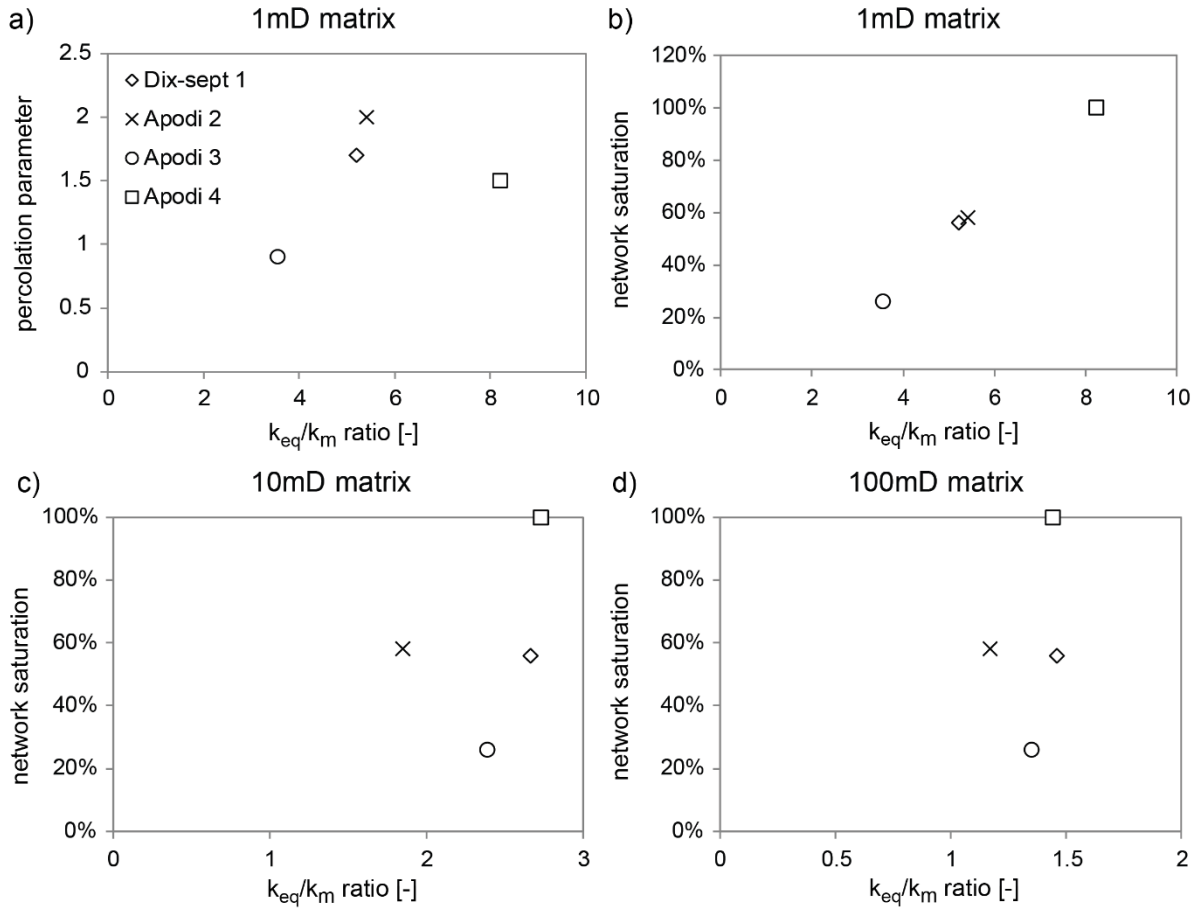

Figure 10 Relation between connectivity and the ratio between equivalent permeability k_{eq} and matrix permeability k_m, derived from the four outcrops: a) Percolation parameter as defined by (Robinson, 1983) *versus equivalent permeability in an impermeable matrix; b) The degree of network saturation derived from cluster analysis versus the equivalent permeability ratio in a 1 mD matrix; c) Network saturation versus permeability ratio for a 10 mD matrix; d) Network saturation versus permeability ratio for a 100 mD matrix.*